Three-Dimensional Basin Depth Map of the Northern Los Angeles Basins from Gravity and Seismic Measurements

Valeria Villa[1], Yida Li[1], Robert Clayton[1], and Patricia Persaud[2]

[1]California Institute of Technology
[2]Louisiana State University

November 23, 2022

Abstract

The San Gabriel, Chino, and San Bernardino sedimentary basins in Southern California amplify earthquake ground motions and prolong the duration of shaking due to the basins' shape and low seismic velocities. In the event of a major earthquake rupture along the southern segment of the San Andreas fault, their connection and physical proximity to Los Angeles can produce a waveguide effect and amplify strong ground motions. Improved estimates of the shape and depth of the sediment-basement interface are needed for more accurate ground-shaking models. We obtain a three-dimensional basement map of the basins by integrating gravity and seismic measurements. The travel time of the sediment-basement P-to-s conversion, and the Bouguer gravity along 10 seismic lines, are combined to produce a linear relationship that is used to extend the 2D models to a 3D basin map. Basement depth is calculated using the predicted travel time constrained by gravity with an S-wave velocity model of the area. The model is further constrained by the basement depths from 17 boreholes. The basement map shows the south-central part of the San Gabriel basin is the deepest part and a significant gravity signature is associated with our interpretation of the Raymond fault. The Chino basin deepens towards the south and shallows northeastward. The San Bernardino basin, bounded by the San Jacinto fault (SJF) and San Andreas fault zone, deepens along the edge of the SJF. In addition, we demonstrate the benefit of using gravity data to aid in the interpretation of the sediment-basement interface in receiver functions.

Three-Dimensional Basin Depth Map of the Northern Los Angeles Basins from Gravity and Seismic Measurements

Valeria Villa[1], Yida Li[1], Robert W. Clayton[1], and Patricia Persaud[2]

[1]California Institute of Technology, Pasadena, CA, 91125.

[2]Louisiana State University, Baton Rouge, LA, 70803.

Corresponding author: Valeria Villa (vvilla@caltech.edu)

Key Points:

- Passive seismic and gravity measurements are combined to estimate the 3D depth of the sediment-basement interface.
- The maximum depth in the San Gabriel basin is 4.5 km, and Chino and San Bernardino basins are less than 2 km deep.
- The trace of the Raymond fault is delineated in the gravity anomaly of the San Gabriel basin.

Abstract

The San Gabriel, Chino, and San Bernardino sedimentary basins in Southern California amplify earthquake ground motions and prolong the duration of shaking due to the basins' shape and low seismic velocities. In the event of a major earthquake rupture along the southern segment of the San Andreas fault, their connection and physical proximity to Los Angeles can produce a waveguide effect and amplify strong ground motions. Improved estimates of the shape and depth of the sediment-basement interface are needed for more accurate ground-shaking models.

We obtain a three-dimensional basement map of the basins by integrating gravity and seismic measurements. The travel time of the sediment-basement P-to-s conversion, and the Bouguer gravity along 10 seismic lines, are combined to produce a linear relationship that is used to extend the 2D profiles to a 3D basin map. Basement depth is calculated using the predicted travel time constrained by gravity with an S-wave velocity model of the area. The model is further constrained by the basement depths from 17 boreholes.

The basement map shows the south-central part of the San Gabriel basin is the deepest part and a significant gravity signature is associated with our interpretation of the Raymond fault. The Chino basin's western side is deeper relative to the eastern side. The San Bernardino basin, bounded by the San Jacinto fault (SJF) and San Andreas fault zone, deepens along the edge of the SJF. In addition, we demonstrate the benefit of using gravity data to aid in the interpretation of the sediment-basement interface in receiver functions.

Plain Language Summary

The shaking levels in the metropolitan area of Los Angeles (LA) due to an earthquake on the San Andreas fault are underestimated. Northeast of LA, the San Gabriel, Chino, and San Bernardino basins influence the amount of shaking the LA area will experience. Sedimentary basins like these can amplify and trap seismic waves. Understanding these basins' shapes will improve our velocity model of the area and therefore seismic hazard estimates. The Basin Amplification Seismic Investigation (BASIN) project deployed several seismic instruments across these basins to characterize subsurface structures. Along with gravity measurements, which capture information about the rock's density variations, we determine the basin depth and shape. The depth model is then combined with the velocity model of the area to produce an improved model. Future shaking models should take these improved models into account.

1.1 Introduction

In the event of a large earthquake rupture, sedimentary basins in the greater Los Angeles area pose a significant seismic hazard. The Los Angeles Basin (LAB) is situated underneath the mega-city of Los Angeles, a metropolitan city with a growing population. Extensive oil and gas exploration in the area provided a rich data set of the subsurface for detailed basin mapping purposes. Northeast of the LAB is the San Gabriel, Chino, and San Bernardino basins. The shape and depth of these basins are not well constrained because of the lack of seismic surveys in the area, particularly active source surveys used for oil and gas exploration. During a large earthquake rupture, the basins trap and amplify seismic waves which highly depend on the thickness, geometry, and material properties of the sedimentary layers within the basin (Frankel, 1993). A wave-guide effect between these northern basins and the LAB is hypothesized. The hypothesized waveguide effect channels the amplified energy towards downtown Los Angeles for events on the southern San Andreas fault (Olsen et al., 2006). Current ground-shaking models in the greater Los Angeles area appear to underestimate the level of ground shaking for earthquakes on the southern segment of the San Andreas fault by a factor of 4 (Denolle et al., 2014). Accurate knowledge of the basin shape and edges will help resolve localized amplification and interference effects (Magistrale et al., 2000).

The primary goal of the Basin Amplification Seismic INvestigation (BASIN) project is to improve the 3D seismic velocity model and structural knowledge of the basins in the northern Los Angeles area. This improved model will help to provide a better estimate of the ground shaking. Here, we integrate results from the BASIN receiver function profiles (Liu et al., 2018; Wang et al., 2021; Ghose et al., 2022) with gravity data and use a 3D seismic velocity (Vs) model obtained from the BASIN dataset (Li et al., 2022) to map the basement depth of the San Gabriel, Chino, and San Bernardino basins. Previous geophysical studies, borehole data, groundwater management reports, and geologic maps are used as additional constraints on the final model. The advantage of this approach is that it allows us to extend the detailed sediment-basement depths from our dense nodal survey to 3D to produce the first integrated basin model for the region.

1.2 Geologic Setting

The San Gabriel basin is a triangular-shaped sedimentary basin bounded by the San Gabriel Mountains on the north, San Jose and Puente Hills on the east, and Repetto and Montebello Hills on the west (Yeats, 2004, Figure 1). The Pliocene-Pleistocene sedimentary fill is comprised of a basal shallow-marine sequence overlain by the non-marine Duarte Conglomerate and underlain by a basement boundary composed of the Peninsular Ranges batholithic and metamorphic rocks such as gneiss (Fuis et al., 2001; Yeats, 2004; Brocher, 2005). Major faults bound the sedimentary fill of the basin with the Sierra Madre fault on the north and Puente Hills blind-thrust in the south (Figure 1b). The west side is marked by the northwest-striking, right-slip East-Montebello fault; and the east side by the northeast-striking, left-slip Walnut Creek fault and Indian Hill fault (Figure 1b). The northeast-striking segment of the Raymond fault separates the deeper San Gabriel basin from the shallower Raymond basin. Wright (1991), Brocher, (2005), and Fuis et al. (2001) estimated the maximum depth of the San Gabriel basin as 3, 3.7, and 5 kilometers (km), respectively. Yeats (2004) inferred the basin trends with a southwest depression towards the Montebello and Repetto Hills and an upward plunge towards the Raymond fault.

The Chino basin is one of the largest groundwater basins in Southern California and the largest in the upper Santa Ana Valley. It is bounded by the Puente Hills on the west, the Jurupa Hills on the southeast, and the San Gabriel Mountains on the north (Figure 1a). The basin is fault bounded by the northeast-striking San Jose fault, northeast-striking Cucamonga fault, southeast-striking Chino fault, and northwestern-striking Rialto-Colton fault (Figure 1b). Tectonic forces uplifted neighboring mountains and depressed the basin along major fault zones (Wildermuth et al., 2005). The depth of groundwater in the northernmost and southernmost parts is less than 152 meters and 4.50 m, respectively, and groundwater movement is north to south (Blomquist, 2021; Dutcher & Garrett, 1963). The bedrock is comprised of a mix of metamorphic, igneous, and consolidated sedimentary rocks.

The San Bernardino basin is a wedge-shaped sedimentary basin bounded by two major fault zones: the San Jacinto Fault zone (SJFZ) to the west and the San Andreas Fault zone (SAFZ) to the east (Figure 1). The San Gabriel and San Bernardino Mountains border the northern and eastern sides of the basin, and on the southern side are the Crafton Hills and Jurupa Hills. The basin's deepest part resembles a pull-apart structure from the Quaternary extension of the major right-step faults of the San Jacinto and San Andreas fault zones (Anderson et al., 2004; Morton & Miller, 2006). The filling of unconsolidated Quaternary and Tertiary alluvial-fan deposits cover the consolidated, non-water bearing Tertiary deposits (Dutcher & Garrett, 1963; Frankel, 1993). The sedimentary section overlies the pre-Tertiary igneous and metamorphic basement rocks (Dutcher & Garrett, 1963). The basement rock types are composed of Peninsular Ranges-type (i.e. granodiorite, quartz diorite, tonalite, and gabbro), San Gabriel Mountains-type (Pelona Schist, and prebatholic crystalline rocks intruded by Mesozoic plutons), Southeastern San Gabriel Complex (i.e. granitic rocks, migmatite, and gneiss), and San Bernardino Mountain-type (Anderson et al., 2004). There are a few basement depths documented from water and oil wells, and records mostly cover the northeastern edges of the basin with a maximum basement depth of around 1.2 km (Dutcher & Garrett, 1963). Stephenson (2002) studied 14 km of seismic reflection data through the San Bernardino area and inferred a depth of 1.7 km near the San Jacinto fault. Anderson et al. (2004) combined gravity and aeromagnetic data to map the San Bernardino basin and found that the largest amount of extension is along the San Jacinto fault with a maximum depth of 2 km. Catchings et al. (2008) found a shallower basin depth (closer to 1.2 km) based on two seismic profiles in the San Bernardino basin.

2 Materials and Methods

2.1 BASIN Project and Receiver Functions

This study integrates seismic and gravity measurements to determine the shape and depth of the San Gabriel, Chino, and San Bernardino basins. The BASIN project deployed approximately 744 seismic nodes from 2017 to 2019, with an average 250-m spacing, across ten seismic lines (Figure 1). The prefix SG is used for lines in the San Gabriel basin and SB for lines in the Chino or San Bernardino basin. Seismic line SB1 crosses all three northern basins and is the longest line. The San Gabriel basin has four lines: SG2, SG1, SG3, and SG4; the Chino basin has three lines: SB4, SB3, and SB5; and the San Bernardino basin has two lines: SB2, SB6, with the basins and lines listed from west to east. The dense intra-line spacing provides the spatial detail used to constrain the basement shape.

Receiver functions (RFs) were computed along the 10 seismic lines by three principal studies within the BASIN project (Liu et al., 2018; Wang et al., 2021; Ghose et al., 2022). These studies concentrated on acquiring the basement-sediment interface, other intra-crustal layers, and the Moho discontinuity, as well as characterizing possible fault offsets. Travel times associated with the sediment-basement interface were determined from the P-S converted phases in the RFs. Liu et al. (2018) applied traditional frequency domain deconvolution to teleseismic events from a 35-day nodal set along SG1, SG2, and SB4 and showed the Moho discontinuity, basement bottom, intermediary sedimentary layers, and offsets along with the Red Hill and Raymond faults. Wang et al. (2021) used a Bayesian array-based coherent receiver function method and multiple events at each station to constrain basin geometry by leveraging the close station-spacing of these short-term dense arrays to aid in suppressing the noise and non-uniqueness of the deconvolution process. The study showed promising lateral layers in the subsurface structure. Ghose et al. (2022) applied a traditional frequency domain deconvolution receiver function method to the nodal dataset, interpreted single-event RF profiles, and showed complex, non-uniform basement topography, evidence of an intra-crustal interface, and a welldefined Moho discontinuity. Detailed information about the BASIN nodal deployment and receiver function work can be found in Clayton et al. (2019) and the respective studies mentioned above.

While these RF studies imaged the sediment-basement interface, there are subtle lateral differences among the studies likely due to noise and rapid lateral variations in the structure. The use of gravity measurements along the lines helps distinguish the sediment-basement interface. In this study, the final time-to-basement is determined from all three RF studies.

2.2 Residual Bouguer Gravity

We extracted Bouguer gravity station data for the northern basins from the Pan-America Center for Earth and Environmental Sciences gravity portal which included four independent gravity measurements (PACES, 2012); Figure S1). The gravity data obtained from PACES (2012) can be downloaded at http://dx.doi.org/10.22002/D1.20256. The Bouguer gravity points were interpolated to a 100-m spacing grid using a nearest-neighbor inverse-distance weighting interpolation scheme to create a Bouguer gravity map of the BASIN study area (Figure 2a). We removed the regional trend from the gravity dataset to isolate the individual basin effects. Geologic knowledge of the area offers insight into how to properly estimate the regional trend. Since the northern basins have different evolutionary histories and distinct strong, nearby gravity signature sources like the Los Angeles basin, we separated the residual calculation for the San Gabriel basin from the Chino and San Bernardino basins. We used information gathered from the geologic map that highlights areas of exposed bedrock (Figure 1a), trends from the RF profiles, and borehole depths (Table S1). The regional trend of the San Gabriel basin was fitted with a second-order polynomial trend that included the San Gabriel Mountains to the north, Repetto Mountains to the south, East Montebello Mountain to the southwest, and Eagle Rock hills to the west while excluding the Los Angeles basin (Figure 1a and 2b). The San Bernardino and Chino residual calculation was computed by fitting a seventh order polynomial over the San Jose Hills to the west, the eastern section of San Gabriel Mountains to the north, San Bernardino Mountains to the east, and Jurupa Hills to the south (Figure 1a and 2c). The regional trend was subtracted from the Bouguer gravity to obtain the residual Bouguer gravity (Figure 2a, 2d).

Residual Bouguer gravity highlights the effect of subsurface density variations, including those due to the topography of the sediment-basement interface. There are different approaches to using residual Bouguer gravity to estimate crustal structure and the depth of sedimentary basins, especially when paired with another geophysical measurement. Tondi et al. (2019) employed a joint inversion of passive seismic and Bouguer gravity data to recover a 3D density model of Northern Italy. Florio (2020) used a depth-gravity relationship where known control points of basement rock depth are related to the residual Bouguer gravity to estimate the thickness of the Yucca flat basin, Nevada.

2.3 Integration of Seismic and Gravity Measurements

We use Bouguer's formula for a basin embedded in a block of thickness H of density ρ_1, and basin of thickness *h* with density ρ_2, given as

$$\delta g = 2\pi G(\rho_1)H + 2\pi G(\rho_2 - \rho_1)h \qquad (1)$$

to linearly relate the gravity anomaly to density and thickness. This establishes a simple linear relationship between the residual Bouguer gravity, δg, and the travel time of the converted phase from the sediment-basement interface, *t*,

$$\delta g = a + bt \qquad (2)$$

where a and b are parameters to be determined by fitting δg to *t*. Expressing equation (1) in the form of equation (2) allows us to relate the residual gravity to the time-to-basement across the basins. Parameter *a* represents the Bouguer gravity of a block of thickness H with density ρ_1. Parameter *b* scales t so that it represents the contributions of a basin of thickness h and density ρ_2 relative to the embedded block. We calculate the parameters using equation (2) with observed Bouguer gravity values and time-to-basement using a least-squares method for each of the ten seismic lines. Since we have gravity values in a three-dimensional mesh, we interpolated the *a* and *b* parameters from the lines to the three-dimensional mesh using an inverse-distance weighted interpolation scheme. We were then able to predict the time-to-basement away from the lines, constrained by the residual gravity anomaly values using the inverted equation (2), $t = (\delta g - a)/\,b$, thus extending from a two-dimensional model to a three-dimensional one.

2.4 Iterative Basement Depth Computation with Shear Wave Velocity Model

Depth to the basement was calculated using the predicted time obtained from equation 2 and a shear wave velocity model (Li et al., 2022). The depth was estimated by assuming vertical incidence for a given Ps or PpPs phase. The Ps phase formula is given by

$$t_{Ps} - t_P = \int_0^h \left(\frac{1}{\beta} - \frac{1}{\alpha}\right) dz \qquad (3)$$

and for the PpPs phase by

$$t_{PpPs} - t_P = \int_0^h \left(\frac{1}{\beta} + \frac{1}{\alpha}\right) dz \qquad (4)$$

where z is depth, *h* is the basin depth, V_s is the S-wave velocity, V_p is the P-wave velocity, t_P is the direct P-arrival time, t_{Ps} the Ps arrival time, and t_{PpPs} is the PpPs arrival time based on the receiver function profiles. S-wave velocities were obtained using an ambient noise cross-correlation approach (Li et al., 2022). S-wave velocities were converted to P-wave velocities using an empirical formula (Brocher, 2005) valid for S-wave velocities between 0 and 4.5 km/s excluding calcium-rich, mafic, gabbros, and serpentine rocks:

$$V_p(km/s) = 0.9409 + 2.0947V_s - 0.8206V_s{}^2 + 0.2683\beta V_s{}^3 - 0.0251V_s{}^4 \quad (5)$$

An initial depth model was calculated using the equation

$$h = \beta\, t_{Ps} \frac{K}{K-1} \quad (6)$$

where K is the V_p/V_s ratio. Equation (6) was derived from (3) and assumes a Ps phase recorded at sea level. We averaged the S-wave velocities across 1 km of the sedimentary column from the initial S-wave velocity model to compute K for each point in the mesh. Initial P-wave velocities were computed using equation (5).

Li et al. (2022) then used the initial depth model as a prior for the shear wave velocity inversion. The inversion of the Vs model is highly dependent on the initial model that uses the basin depth as a constraint. Using the shear wave velocity results, the depth was recalculated using equations (3) or (4) depending on which converted phase is used. A linear relationship between the modeled depth and the predicted time-to-basement was established to fill in for the few points in the mesh that did not converge. We used an iterative process instead of solving an inverse problem because of the nonlinearity of the method. The prior basin model was provided for the Vs inversion and the new Vs model for the depth model calculations.

The algorithm outputs the estimated basement depth when the difference between S-wave travel time and P-wave travel time (3) or when the sum of S and P wave travel time (4) approximately equaled the sediment-basement interface time based on the RF studies. For the San Gabriel basin, we assumed a primary phase, Ps, while for the Chino and San Bernardino basins a PpPs phase. Our justification for using a PpPs phase was based on the shallower sedimentary basin (< 2 km) obtained with equation (4) that agrees well with other independent sources. For instance, two boreholes in the Chino basin support a basin shallower than 2 km. The Chino Basin Management report by Wildermuth et al. (2005) showed multiple (>50) boreholes that penetrated sedimentary and crystalline basements at shallow depths (< 2 km; see Wildermuth et al. (2005) report for exact boreholes locations). Two boreholes not associated with groundwater monitoring showed depths less than 1 km (Table S1). In addition, multiple studies in the San Bernardino basin indicate measured depths of less than 2 km as mentioned in Section 1.2.

2.5 Integration of Borehole Basement Depths

Multiple borehole logs with recorded basement depth allowed us to constrain and corroborate our final depth model. There is a total of 17 borehole logs with recorded basement depths: 11 in the San Gabriel basin, 2 in the Chino basin, and 4 in the Raymond basin (Table S1). Because the Chino basin contains only two borehole measurements, we assessed the model based on the closeness to the recorded depth and shifted all points in the Chino and SB basin mesh 500 m down to match the boreholes and previous maximum depths found in studies mentioned in Section 1.2. Borehole measurements provided another advantage in areas of poor interpolation of the inversion parameters. Such is the case in the Raymond basin where the interpolated parameters from equation (2) are influenced by the gravity response and time-to-basement of SG2. It is difficult to evaluate this basin based on the response of SG2 because this line crosses the deeper SG basin and the edge of the Raymond basin. Thus, the depths in this area were estimated using this quadratic depth-gravity relation using 4 control borehole points (Table S1) obtained from the Buwalda (1940) report.

3 Results

3.1 Time-to-Basement and Residual Bouguer Gravity Profiles

Figures 3 to 4 show the final basement interpretations for SG2 and SG1 and the results from two RF studies. Results for SG3 and SG4 are shown in Figure S2. All four lines show a good linear relationship between the time-to-basement and the residual Bouguer gravity. The sediment-basement boundary interpretation along lines SG2 and SG4 were modified based on the geological interpretations of the gravity signatures and/or other factors which will be discussed later. Lines SG1 and SG3 followed Wang et al. (2022) interpretation of the sediment-basement interface. The part of SB1 in the San Gabriel basin was reinterpreted based on Wang et al. (2021) and Ghose et al. (2022). The SG2 line crosses the intersection of the Eagle Rock fault and the Raymond fault (Figure 3). The change in topography associated with the fault scarp is evident in the gravity profile of SG2 which shows a steep gradient dipping to the south (Figure 3b). The East Montebello fault runs near parallel to SG2 and merges the Raymond fault. The SB1 line intersects the East Montebello fault, and a significant gravity gradient is also present near the steep gradient found along SG2.

All sediment-basement interfaces in the Chino basin were reinterpreted following Wang et al. (2021), Ghose et al. (2022), and gravity trends. Figure 5 shows the SB4 profile with large negative residual Bouguer gravity values and longer basement-time to the north. The SB3 and SB5 lines are shown in figures S3 and S4. The SB3 profile shows the opposite trend with lower gravity values and larger times to the south relative to the north. The gravity lows between each north and south section of the lines are lower in the SB4 line than in the SB3. The SB5 profile depicts a similar trend to that observed along SB4, with negative values concentrated to the north, abutting the San Gabriel Mountains. In contrast to the SB4 and SB3 lines, the SB5 line shows a negative value that curves upwards to positive values and then gradually decreases to the south. The depression in the south has higher gravity values than those in the north.

The San Bernardino basin lines (SB2 and SB6) have a good correlation between negative gravity values and longer travel time-to-basement along the San Jacinto Fault (SJF) (Figure 6 and S5). The SB2 profile follows Wang et al. (2021) version of the sediment-basement interface and SB6 follows Ghose et al. (2022) values. It should be noted that Ghose et al. (2022) picks on SB2 agreed with the Wang et al. (2021) values except for the northern section. The southern section of SB2 shows the lowest gravity values in the basin and the time reflects this trend. The SB6 line also reflects this trend based on the lower negative values to the east of the line, which ends near the SB2 line.

3.2 3-D Residual Bouguer Gravity Model

The residual Bouguer gravity for the San Gabriel basin shows prominent gravity signatures over faults, mountains, and basins. A steep gravity gradient extends 10 km from Repetto Hills toward the Sierra Madre fault, which aligns well with the mapped Raymond fault trace (Figure 1b). A smaller triangular block extending northwest of the intersection of the Eagle Rock fault and the Raymond fault shows the highest gravity values in the San Gabriel basin and is assumed to be caused by the Repetto Hills and associated exposed conglomerate and sandstone of the Topanga

Group (Yerkes & Campbell, 2005, Figure 1b). Another gravity gradient trending northwest strikes subparallel to the East Montebello fault. The northern central part of the San Gabriel basin shows high gravity values that extend eastward towards SG4. The southern central part shows the lowest gravity values in the basin. Gravity highs increase steadily from the central lows towards SG3 between the San Jose Hills and the San Gabriel Mountains (SG4), which is marked by a channel-like feature in the gravity anomaly.

Gravity highs are encountered in the east and lows in the west of the Chino basin. The location of SB3 represents a close approximation of this division in gravity values (Figure 1b). The highest positive values are in the southeast and are likely due to the exposed basement in the Jurupa Hills composed of quartz-biotite gneiss, impure quartzite, biotite-quartz schist, marble, calc-silicate contact rocks, and amphibole schist (MacKevett, 1950, Figure 1a), that produce a positive density contrast against the low-density basin fill. In the southern segment of SB3, there are negative values surrounded by positive values. The Jurupa Valley is approximately located near these negative values. These lower density sediments from the Jurupa Valley are contrasted against the exposed Jurupa Hills rocks to the northeast-east and older alluvium-fan deposits to the west. A strong gravity gradient signature divides the Chino basin and San Bernardino basins. This strong gravity gradient correlates well with the SJFZ, a series of right-lateral strike-slip faults (Figure 1b).

The lowest gravity values associated with the San Bernardino basin are along the SJF. The gravity values then increase towards the root of the San Bernardino Mountain and the SAF. The higher gravity values are due to the metamorphic basement rock composition of the San Bernardino Mountains. The low values are associated with the basin fill comprised of unconsolidated Quaternary and Tertiary alluvial-fan deposits overlying the consolidated, non-water bearing Tertiary deposits. The lower gravity values in the northern part of the San Bernardino basin might be explained by the southeastern San Gabriel Complex, likely from the black belt of the magnetic mylonitic rocks (Anderson et al., 2004; Nourse, 2002).

3.3 3D Basin Depth Map Model

Figure 7 shows the final basement depth model for the northern Los Angeles basins. The San Gabriel basin is triangular shaped and bounded by the Raymond fault to the northwest, the Sierra Madre fault to the north, the San Jose fault to the east, and the East Montebello fault to the west. The Raymond fault separates the Raymond basin from the San Gabriel basin and acts as an impermeable barrier (Buwalda, 1940). The Raymond basin has depths up to 365 m. The Raymond fault shows potential vertical offset with a change in basement depth of nearly 1 km across the fault. The Sierra Madre fault shows three spatial barriers of varying depth based on the basin depth map: one near the boundary of the Raymond basin, a central deeper segment near borehole 7, and a shallower depth offset between SG3 and SG4. The San Jose fault is mapped in an area of shallow basement depths. The East Montebello fault is in a region of uplift in the north and subsidence in the south. Basement depths are shallow near the Eagle Rock and Raymond fault intersection and decrease southeastwards towards Montebello, CA. At the southern end of SG1, there is an uplift that might extend further south towards the Montebello Hills. East of this uplift near SG3, the basin resumes depths of 3-4.5 km, which continue throughout most of the basin.

The Chino basin is deeper east of SB4 and has shallower depths around the SB3 and SB5 lines. The deeper areas are two regions with 2-2.5 km basement depth within an irregularly shaped area of shallower basement (1-1.5 km depth). The SB3 line shows sedimentary layers with varying thicknesses. The SB3 is slightly deeper in the south relative to the north. The 3D map depicts this southward deepening trend merging to the 1-1.5 km deep irregular shape previously mentioned. Basement depths are much shallower along SB5 compared to SB3 and SB4. These shallower depths are likely due to the Jurupa Hills in the south (Figure 1b). Unlike the southern segment, the northern segment of SB5 is deeper and dips east northward.

Basement topography in the San Bernardino basin reveals a clear pattern of subsidence along the SJFZ. Figure 6 shows the SB2 depth profile deepening towards the south near the SJFZ and shallowing towards the SAF and the San Bernardino Mountains. Similarly, the basement along the SB6 profile deepens to the west towards the SB2 (Figure S5). The estimated basement depth map for the San Bernardino basin shows depths of ~2 km along the southern part of the SJFZ. The basement depths increase gradually to 1 km towards the San Bernardino Mountains and the SAF. There exists a separate deeper region with depths close to 2 km towards the north of the SJFZ. This area extends to the west of the Chino basin and is observed in the northern segment of the SB5 line as previously described.

3.4 Basement Depths Uncertainty

The uncertainty of the basement depths might be due to rocks within the basin with different densities, the misfit between the predicted and observed residual Bouguer gravity due to shorter wavelength geologic features not included in the model, or the uncertainties in the velocity model. While extensive work was done to remove the regional trend from the Bouguer gravity values to ensure they represent the basin fill, there were areas where we could not capture all local effects within the basin. Line SG4 shows this uncertainty and is discussed in Section 4. Furthermore, the Vs model has areas of low ray path coverage which might result in outliers affecting the depth calculation. The southern part of SB3 best illustrates this uncertainty and is discussed in Section 4. Another source of uncertainty is reflected in the predicted time-to-basement that may correspond to a negative RF phase instead of a positive phase like Ps or PpPs. A possible reason for this is the predicted time constrained by gravity comes with uncertainties such as those mentioned above but is also dependent on density contrasts and a and b parameters. In contrast, the RF conversions reflect impedance contrasts suggesting that there are instances where the two may not match. Nevertheless, the inversion for the time-to-basement is more sensitive to the b parameter than other inversion parameters.

4 Discussion

Here we discuss the interpretation of the sediment-basement interface based on the sources of the gravity anomalies and the time-to-basement and how these interpretations along with borehole data aided our final basement depth map for each basin. Table S1 summarizes the borehole data and drilled basement depths used to constrain the final basin model.

The San Gabriel basin reveals a triangular-shaped basement bounded by major strike slips and thrust faults. The most prominent gravity gradient in the San Gabriel basin aligns with the trace of the left-lateral strike-slip Raymond fault. The source of this gravity anomaly is likely due to the offset of basement ridges, which juxtaposes blocks with different basement elevations. Weaver and Dolan (2000) reported a 3.4 km left-lateral offset of a crystalline basement ridge at the east end of the Raymond fault. The Raymond fault separates the Raymond and the San Gabriel basins. While the Raymond basin is included in the model, there are insufficient nodal stations located there aside from the northern part of SG2, to constrain the Raymond basin and the residual Bouguer gravity might not capture the local effects of this shallower basin in comparison to the larger and more prominent San Gabriel basin. The majority of our interpretation of the Raymond basin comes from Buwalda (1940) where it was concluded that the Raymond fault acts as an impermeable barrier between the shallower Raymond basin and the San Gabriel basin. Estimated depths of the Raymond basin range from 250 to 1000 m.

Another gravity high within the San Gabriel basin study region is observed near Eagle Rock, Raymond, and East Montebello faults intersection. Near the intersection, we observe a steep gravity gradient signature along the SG2 and SB1 lines (Figure 2d, 3). The source of this gravity high may be explained as a result of a restraining bend from the Raymond fault (Weaver & Dolan, 2000). East of the intersection, the source is attributed to the displacement of old crystalline rocks of the San Rafael Hills from the Tertiary rocks (Buwalda, 1940). Due to the prominent gravity signatures that delineate the traces of faults, we reinterpreted the sediment-basement interface in the time-to-basement profile to reflect this sharp steep gradient that is not reflected in the RF profiles.

The third gravity high aligns with the East Montebello fault, which runs parallel to SG2. While this fault bounds the southwest boundary of the San Gabriel basin and separates it from the Los Angeles basin, the sedimentary layer thickness is not consistent along the strike of the fault or the SG2 line. Basement depths closer to 2 km in its southern segment and 1 km to the north suggest the East Montebello fault may not be a purely right-slip fault but may have a component of non-uniform vertical separation along strike, allowing more accommodation space to be created at its southern end. Yeats (2004) found the southwestern part of the East Montebello fault was subsiding more than the northeast area. In addition to the East Montebello fault interpretation, the positive residual gravity values also likely reflect the Repetto Hills which were uplifted by the Elysian Park anticlinorium (Dolan et al., 2001).

The central segment of the San Gabriel basin depth map (Figure 7) is divided into two deeper sedimentary sections by a central high near the middle of the SG1 line intersection. Figures 4 and S3 show a uniform increase in sedimentary layer thickness towards the south, suggesting a deeper southern basin. However, the southern end of SG1 also shows a slight decrease in thickness, which is attributed to the Hacienda Hills. Along the southern rim of the San Gabriel basin, the Repetto Hills are located to the west and the Hacienda and Puente Hills are located on the central and east-central sides. The easternmost end of the basin, however, shows a deepening along the left-lateral Walnut Creek fault. While the Walnut Creek fault shows no tectonic geomorphic expression, it separates the flat-lying strata of the San Gabriel basin from folded strata of the San Jose and Puente Hills (Yeats, 2004).

The connection between the San Gabriel and the Chino basins is best illustrated using our interpretation of the SG4 line (Figure S2). Due to its proximity to both the San Gabriel and Chino basin, this line provides insight into the edges of both basins. Evaluating the 3D basin depth map around this region we find that this area acts more as a saddle with a decrease in depth from the west to an increase in depth to the east and then a gradual decrease further east. The slope in basement topography is more gradual towards the Chino basin and steeper towards the San Gabriel basin. This is an important factor when determining the impact of the channeling waveguide effect of a seismic event. However, there is large uncertainty in the sediment-basement interpretation due to conflicting RF interface interpretations and residual gravity values along the SG4 line.

The SG4 sediment-basement interface from the RF studies was reinterpreted due to opposing gravity and RF slopes since slopes need to have the same sign for proper time-to-basement inversion. The RF studies from Ghose et al. (2022) and Wang et al. (2021) show time-to-basement increasing to the south, with Wang et al. (2021) having slightly larger values in the south (Figure S2e). The gravity signature, however, showed the gravity decreasing northwards, towards the base of the San Gabriel Mountains (Figure S2f). It is quite possible that the residual gravity computation did not completely remove the edge effects or possible local wavelength features of the Indian Hill fault. For example, the different polynomial trends applied to estimate the regional trend for the San Gabriel and Chino, and San Bernardino basin might create sharp discontinuities in the residual gravity map. Two further steps were taken to ensure inversion of the time-to-basement in this area. Instead of taking the SG4 line as the edge of the San Gabriel basin, we used it as a blending tool for both residual calculations by extending a few kilometers eastward or westward, respectively for each basin (Figure 2b, c). In essence, this ensured the SG4 line had similar residual Bouguer gravity values from two different regional trends subtraction. We then purposely reinterpreted the SG4 time-to-basement to ensure a shallower interpretation of the predicted time, as similar as possible to the actual RF times. The predicted time constrained by gravity follows closely the established RF times in the north but with a distinction of shorter times in the south. When evaluating this depth profile, the northern end is better resolved than the southern end.

The Chino basin is deeper in the west and shallower in the east. A shallower north-south trending segment is present east of SB4 and is likely attributed to the exposed bedrocks of the Jurupa Hills in the south. The two deeper pockets, which are also highlighted by gravity lows, are near the city of Upland and Chino. The basin shallows to 1 km towards the SB3 and SB5 lines. The basin depth map has very shallow depths south of SB5 where the Jurupa Hills are located. Slightly southwest of this, we find the Jurupa Valley which our model depicts as a deeper region as shown in the SB3 line. While the basin topography in the center of the Chino basin does not allow outright unequivocal interpretations, borehole data corroborated the deeper trend toward the west (Wildermuth et al., 2005). The Wildermuth et al. (2005) report describes a series of boreholes that penetrate crystalline bedrock in the east and sedimentary bedrock in the west at similar drilling depths, suggesting a deeper west. The shallower eastern side relative to the deeper western part of the Chino basin in the model reflects the shallower crystalline basement captured in the boreholes.

The estimated basement shape of the San Bernardino basin suggests a pull-apart basin structure described by extension along major fault zones. The strand of the San Jacinto fault running through the San Bernardino basin is called the Claremont strand. There is ~2 km subsidence associated with this strand of the SJF. The choice for the sediment-basement interface favors a shallower interpretation for the SB6 line, which follows Ghose et al. (2022) and is consistent with the intersection with SB2. This diverges from Wang et al. (2021) results, which Ghose et al. (2022) interpret as an intra-crustal layer. The different interpretations of the sediment-basement interface for SB2 between Ghose et al. (2022) and Wang et al. (2021) is the northern segment; with Ghose et al. (2022) favoring a deeper structure while Wang et al. (2021) show a thinner sedimentary layer of more uniform thickness. The gravity profile resembles the flat structure of Wang et al. (2021), but it should be noted that the velocity model (Figure 6d) reveals a low-velocity zone near Ghose et al. (2022) zone of subsidence. The depth profile constrains the northern segment to a shallower depth than the southern segment which is bounded by the Claremont strand. A possible reason for the discrepancy might be due to the exposed bedrock to the northwest of the SB2 line. The regional trend removed the effects of the San Bernardino Mountains, but it is possible that the effects from the exposed bedrock within the basin were not well resolved.

5 Conclusion

The 3-D shape and depths of the northern Los Angeles basins were computed by integrating seismic and Bouguer gravity measurements along with the surface and borehole geology. Due to the densely spaced constraints along 10 individual seismic lines, this approach was effective at determining the detailed geometry of the sediment-basement interface in an ~90-km wide region extending from the southern SAF to downtown Los Angeles. Model validation against 17 borehole recorded basement depths allowed us to address non-uniqueness and trade-offs between seismic velocities and travel times. Gravity measurements constrained the 3-D shape of the sediment-basement interface and delineated the effects of faults around the basins. The basement shape and depths further contributed to improving a 3-D basin-scale velocity model as a prior (Li et al., 2022). The triangular-shaped San Gabriel basin is a fault-bounded basin with a maximum depth of 4.5 km in its western and easternmost centers. The Chino basin is broader and substantially shallower than the San Gabriel basin and dominated by a 1.5-2 km thick sedimentary layer in its western segment. The San Bernardino basin exhibits ~2 km subsidence along the Claremont strand of the SJF, consistent with a pull-apart structure. Further work on ground motion simulations is needed to evaluate the seismic hazard and risk of the northern Los Angeles basins and improve ground shaking models for large earthquake ruptures such as the forecasted M_w 7.8 on the southern San Andreas fault.

Acknowledgments

We are grateful to the hundreds of nodal deployment volunteers, Los Angeles residents, and business owners who hosted our instruments. We thank Liu et al. (2018), Wang et al. (2021), and Ghose et al. (2022) for providing their receiver function results. This research was supported by the National Science Foundation awards 2105358 and 2105320. The BASIN project was partly supported by U.S. Geological Survey awards GS17AP00002 and G19AP00015, and Southern California Earthquake Center awards 18029 and 19033. Data collection was supported by Louisiana State University and California Institute of Technology. Nodal instruments were provided by Incorporated Research Institutions for Seismology (IRIS), Portable Array Seismic Studies of the Continental Lithosphere (PASSCAL), University of Utah, Louisiana State University, and the University of Oklahoma.

Data Availability Statement

The basement time was obtained from Liu et al. (2018), Wang et al. (2021), and Ghose et al. (2022). Li et al. (2022) provided the shear-wave velocity model. The basement depths obtained from well logs are publicly available through the Geologic Energy Management Division's (CalGEM) online mapping application Well Finder https://www.conservation.ca.gov/calgem/Pages/WellFinder.aspx and Buwalda (1940). The Bouguer gravity data was provided by the Pan American Center Earth and Environmental Science portal. Figures were plotted using the GMT software, PyGMT, and cartopy (Met Office, 2010; Uieda et al., 2022; Wessel et al., 2019). The 3D basin depth model is available at http://doi.org/10.22002/D1.20252.

References

Anderson, M., Matti, J., & Jachens, R. (2004). Structural model of the San Bernardino basin, California, from analysis of gravity, aeromagnetic, and seismicity data: STRUCTURE OF THE SAN BERNARDINO BASIN. *Journal of Geophysical Research: Solid Earth*, *109*(B4). https://doi.org/10.1029/2003JB002544

Blomquist, W. (2021). The Natural Physical System of Chino Basin. In W. Blomquist, *The Realities of Adaptive Groundwater Management* (Vol. 27, pp. 13–21). Springer International Publishing. https://doi.org/10.1007/978-3-030-63723-1_2

Brocher, T. M. (2005). Empirical Relations between Elastic Wavespeeds and Density in the Earth's Crust. *Bulletin of the Seismological Society of America*, *95*(6), 2081–2092. https://doi.org/10.1785/0120050077

Buwalda, J. P. (1940). *Geology of the Raymond Basin* (pp. 1–131). California Institute of Technology. http://doi.org/10.22002/D1.20258

Catchings, R. D., Rymer, M. J., Goldman, M. R., Gandhok, G., & Steedman, C. E. (2008). *Structure of the San Bernardino Basin along two seismic transects: Rialto-Colton Fault to the San Andreas Fault and along the I-215 Freeway (I-10 to SR30)* (Report No. 2008–1197; Version 1.0, Open-File Report). USGS Publications Warehouse. https://doi.org/10.3133/ofr20081197

Clayton, R., Persaud, P., Denolle, M., & Polet, J. (2019). Exposing Los Angeles's Shaky Geologic Underbelly. *Eos*, *100*. https://doi.org/10.1029/2019EO135099

Denolle, M. A., Dunham, E. M., Prieto, G. A., & Beroza, G. C. (2014). Strong Ground Motion Prediction Using Virtual Earthquakes. *Science*, *343*(6169), 399–403. https://doi.org/10.1126/science.1245678

Dolan, J. F., Gath, E. M., Grant, L. B., Legg, M., Lindvall, S., Mueller, K., Oskin, M., Ponti, D. F., Rubin, C. M., Rockwell, T. K., H, J., Treiman, A., Walls, C., & Yeats (compiler, R. S. (n.d.). *1 Active Faults in the Los Angeles Metropolitan Region Southern California Earthquake Center Group C**.

Dolan, J. F., Gath, E. M., Grant, L. B., Legg, M., Lindvall, S., Mueller, K., Oskin, M., Ponti, D. F., Rubin, C. M., Rockwell, T. K., Treiman, A., Walls, C., & Yeats, R. S. (2001). *Active Faults in the Los Angeles Metropolitan Region* (SCEC Special Pub Southern California Earthquake Center Group C; No. 001, p. 47). Southern California Earthquake Center. http://scecinfo.usc.edu/research/special/SCEC001activefaultsLA.pdf

Dutcher, L. C., & Garrett, A. A. (1963). *Geologic and hydrologic features of the San Bernardino area, California; with special reference to underflow across the San Jacinto fault*. https://doi.org/10.3133/wsp1419

Florio, G. (2020). The Estimation of Depth to Basement Under Sedimentary Basins from Gravity Data: Review of Approaches and the ITRESC Method, with an Application to the Yucca Flat Basin (Nevada). *Surveys in Geophysics*, *41*(5), 935–961. https://doi.org/10.1007/s10712-020-09601-9

Frankel, A. (1993). Three-dimensional simulations of ground motions in the San Bernardino Valley, California, for hypothetical earthquakes on the San Andreas fault. *Bulletin of the Seismological Society of America*, *83*(4), 1020–1041. https://doi.org/10.1785/BSSA0830041020

Fuis, G. S., Ryberg, T., Godfrey, N. J., Okaya, D. A., & Murphy, J. M. (2001). Crustal structure and tectonics from the Los Angeles basin to the Mojave Desert, southern California. *Geology*, *29*(1), 15–18. https://doi.org/10.1130/0091-7613(2001)029<0015:CSATFT>2.0.CO;2

Ghose, R., Persaud, P., Wang, X., & Clayton, R. W. (2022). *High-frequency receiver function profiles reveal sedimentary basin structure beneath the northern Los Angeles area* [In-preparation].

Li, Y., Villa, V., Clayton, R., & Persaud, P. (2022). *Shear Wave Velocities in the San Gabriel and San Bernardino Basins, California* (world). https://doi.org/10.1002/essoar.10512118.1

Liu, G., Persaud, P., & Clayton, R. W. (2018). Structure of the Northern Los Angeles Basins Revealed in Teleseismic Receiver Functions from Short-Term Nodal Seismic Arrays. *Seismological Research Letters*, *89*(5), 1680–1689. https://doi.org/10.1785/0220180071

MacKevett, E. M. (1950). *The geology of the Jurupa Mountains, San Bernardino and Riverside Counties, California* [Masters, California Institute of Technology]. https://doi.org/10.7907/Y1V7-CG63

Magistrale, H., Day, S. M., Clayton, R. W., & Graves, R. (2000). The SCEC Southern California Reference Three-Dimensional Seismic Velocity Model Version 2. *Bulletin of the Seismological Society of America*, *90*(6B), S65–S76. https://doi.org/10.1785/0120000510

Met Office. (2010). *Cartopy: A cartographic python library with a matplotlib interface*. http://scitools.org.uk/cartopy

Morton, D. M., & Miller, F. K. (2006). *Geologic Map of the San Bernardino and Santa Ana 30' x 60' quadrangles, California* [Map]. https://pubs.usgs.gov/of/2006/1217/

Nourse, J. A. (2002). Middle Miocene reconstruction of the central and eastern San Gabriel Mountains, southern California, with implications for evolution of the San Gabriel fault and Los Angeles basin. In A. Barth, *Contributions to Crustal Evolution of the Southwestern United States*. Geological Society of America. https://doi.org/10.1130/0-8137-2365-5.161

Olsen, K. B., Day, S. M., Minster, J. B., Cui, Y., Chourasia, A., Faerman, M., Moore, R., Maechling, P., & Jordan, T. (2006). Strong shaking in Los Angeles expected from southern San Andreas earthquake. *Geophysical Research Letters*, *33*(7). https://doi.org/10.1029/2005GL025472

PACES. (2012). Pan-American Center for Earth and Environmental Studies. http://gis.utep.edu/paces/PACES%20Gravity%20Magnetics.htm

Stephenson, W. J. (2002). Delineation of Faulting and Basin Geometry along a Seismic Reflection Transect in Urbanized San Bernardino Valley, California. *Bulletin of the Seismological Society of America*, *92*(6), 2504–2520. https://doi.org/10.1785/0120010222

Tondi, R., Vuan, A., Borghi, A., & Argnani, A. (2019). Integrated crustal model beneath the Po Plain (Northern Italy) from surface wave tomography and Bouguer gravity data. *Tectonophysics*, *750*, 262–279. https://doi.org/10.1016/j.tecto.2018.10.018

Uieda, L., Tian, D., Leong, W. J., Jones, M., Schlitzer, W., Grund, M., Toney, L., Yao, J., Magen, Y., Materna, K., Newton, T., Anant, A., Ziebarth, M., Quinn, J., & Wessel, P. (2022). *PyGMT: A Python interface for the Generic Mapping Tools* (v0.7.0). Zenodo. https://doi.org/10.5281/zenodo.6702566

Wang, X., Zhan, Z., Zhong, M., Persaud, P., & Clayton, R. W. (2021). Urban Basin Structure Imaging Based on Dense Arrays and Bayesian Array-Based Coherent Receiver Functions. *Journal of Geophysical Research: Solid Earth*, *126*(9). https://doi.org/10.1029/2021JB022279

Weaver, K. D., & Dolan, J. F. (2000). Paleoseismology and Geomorphology of the Raymond Fault, Los Angeles County, California. *Bulletin of the Seismological Society of America*, *90*(6), 1409–1429. https://doi.org/10.1785/0119990075

Wessel, P., Luis, J. F., Uieda, L., Scharroo, R., Wobbe, F., Smith, W. H. F., & Tian, D. (2019). The Generic Mapping Tools Version 6. *Geochemistry, Geophysics, Geosystems*, *20*(11), 5556–5564. https://doi.org/10.1029/2019GC008515

Wildermuth, M. J., LeClaire, J. P., Malone, A. E., Hwang, J. H., Rossi, J. V., & Atwater, R. (2005). *Chino Basin Optimum Basin Management Program* (pp. 1–12). https://doi.org/10.1061/40763(178)140

Wright, T. L. (1991). *Chapter 3 Structural Geology and Tectonic Evolution of the Los Angeles Basin, California*. https://doi.org/10.1306/M52531C3

Yeats, R. S. (2004). Tectonics of the San Gabriel Basin and surroundings, southern California. *Geological Society of America Bulletin*, *116*(9), 1158. https://doi.org/10.1130/B25346.1

Yerkes, R. F., & Campbell, R. H. (2005). *Preliminary Geologic Map of the Los Angeles 30' x 60' Quadrangle, Southern California* [Map]. U.S. Geological Survey. https://pubs.usgs.gov/of/2005/1019/

Figures

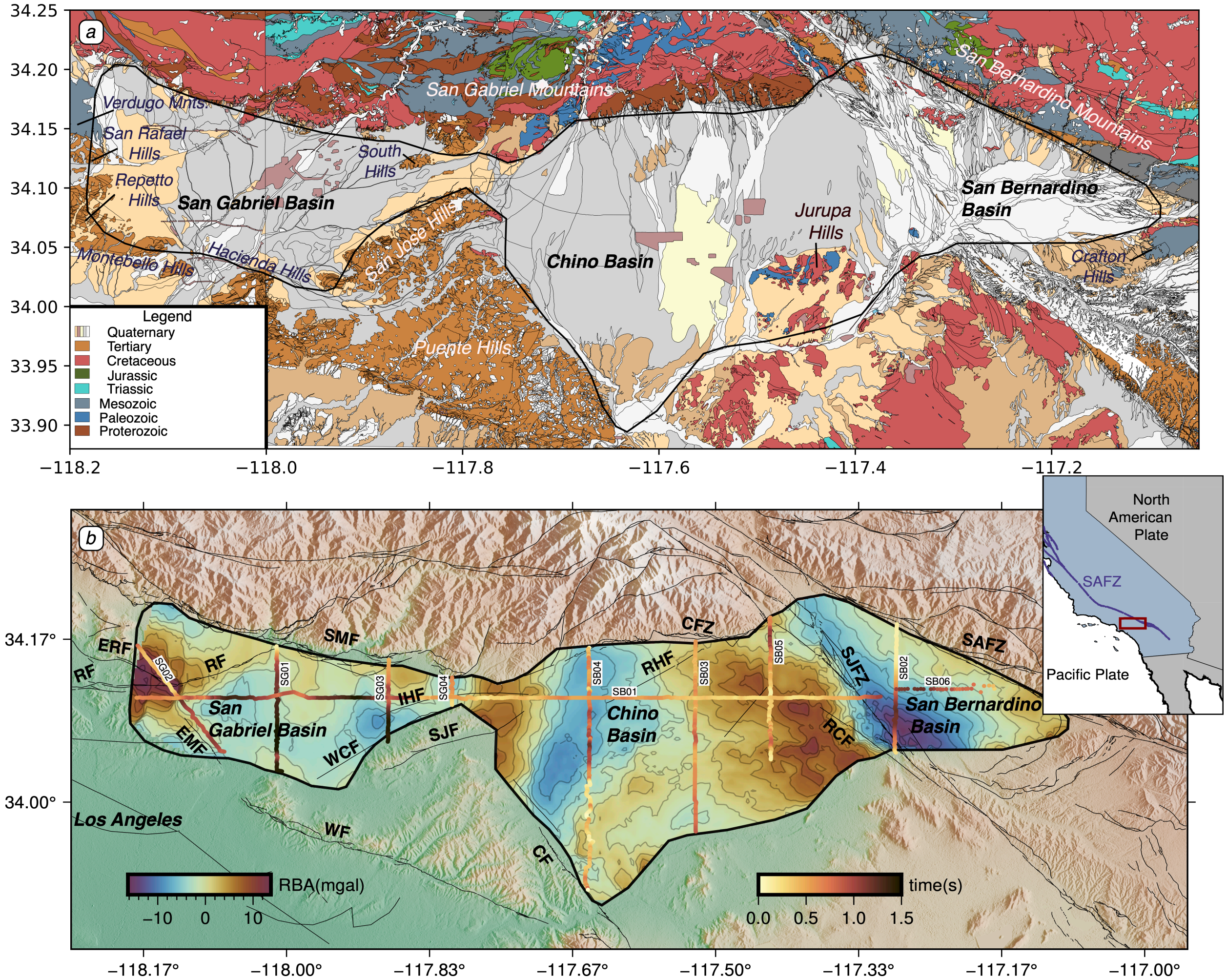

Figure 1. (a) Geologic map of the northern Los Angeles basins. The geologic age of the units is shown in the legend. Adapted from Yerkes and Campbell (2005) and Morton and Miller (2006). (b) Shaded-relief terrain map showing the outline of the BASIN survey. The contoured grid depicts the residual Bouguer gravity. Dark red-yellow-white circles show the time-to-basement in seconds along the 10 node lines. Black thin lines are fault locations. CF, Chino Hill Fault; CFZ, Cucamonga Fault Zone; EMF, East Montebello Fault; ERF, Eagle Rock Fault; IHF, Indian Hill Fault; RCF, Rialto Colton Fault; RF, Raymond Fault; RHF, Red Hill Fault; SJF, San Jose Fault; SJFZ, San Jacinto Fault Zone; SMF, Sierra Madre Fault; WCF, Walnut Creek Fault; WF, Whittier Fault;

SAFZ, San Andreas Fault Zone. The inset map outlines the study area concerning the transform plate boundary between the Pacific and North American plates.

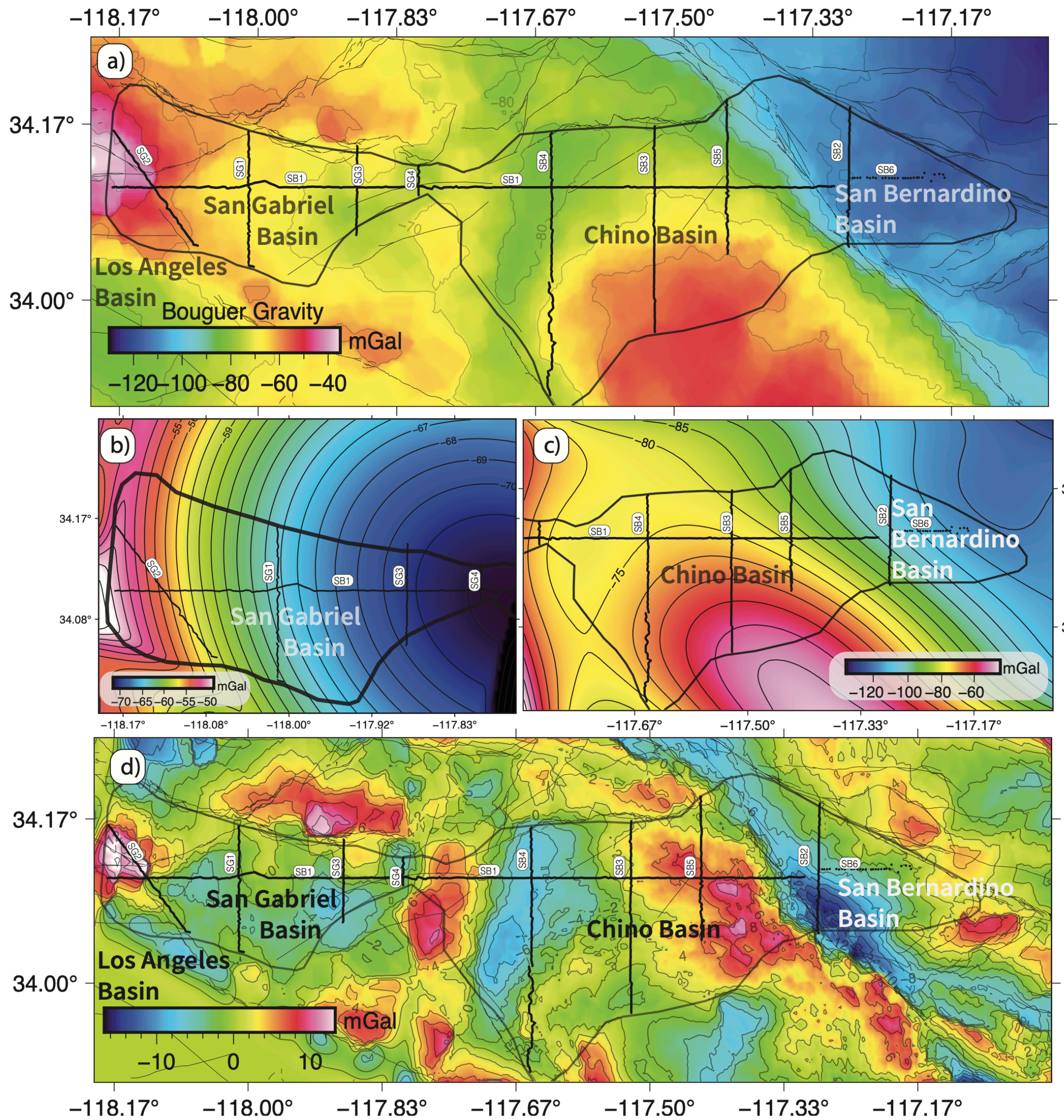

Figure 2. (a) Map of Bouguer gravity of the San Gabriel, Chino, and San Bernardino basins obtained from the *PACES* (2012) portal. (b) 2nd order polynomial trend for San Gabriel basin. (c)

7th order polynomial trend for Chino and San Bernardino basins. (d) Residual Bouguer anomaly map. The black outline shows the study area. Black lines represent the 10 nodal BASIN lines.

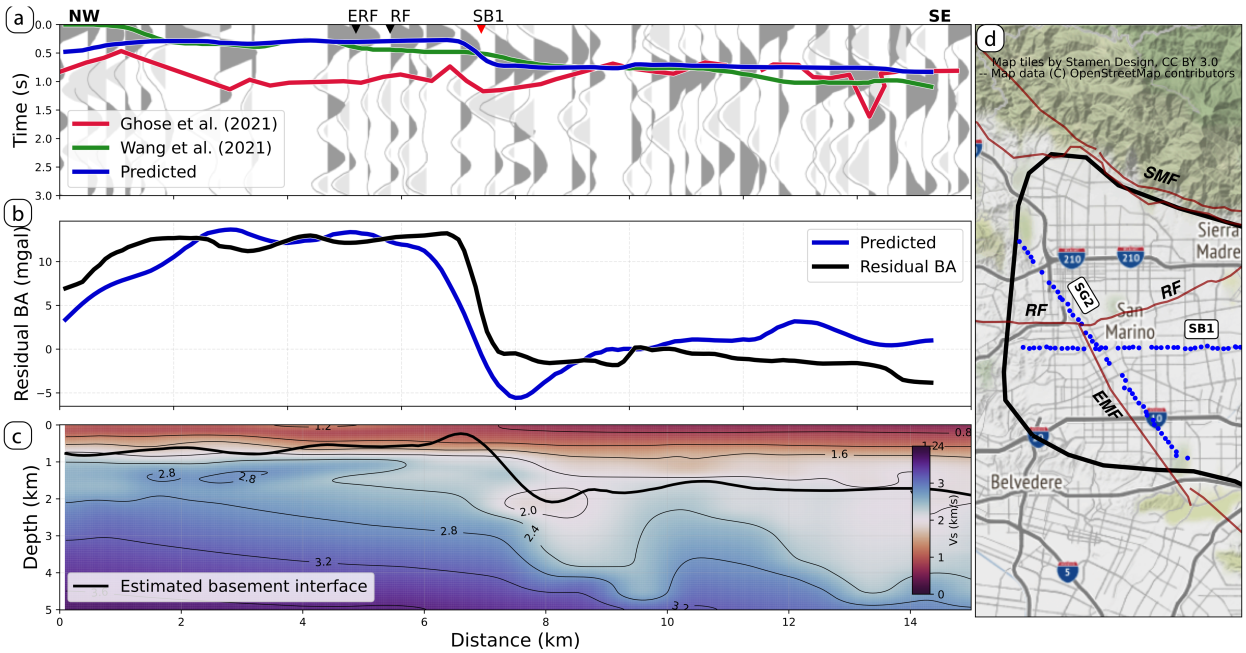

Figure 3. a) Profile along SG2 showing the time-to-basement from two RF studies and the predicted time-to-basement from this study. RF background from Ghose et al. (2022) is from a single event. b) Residual and predicted Bouguer anomaly is shown with black and blue lines, respectively. c) Shear wave velocity cross-section from Li et al. (2022) and the estimated basement surface determined by converting the blue line in a) to depth. d) Map showing the nodal stations of the SG2 line as blue dots. SB1 stations are included for reference. Maroon lines are fault locations. EMF, East Montebello fault; SMF, Sierra Madre fault; RF, Raymond fault.

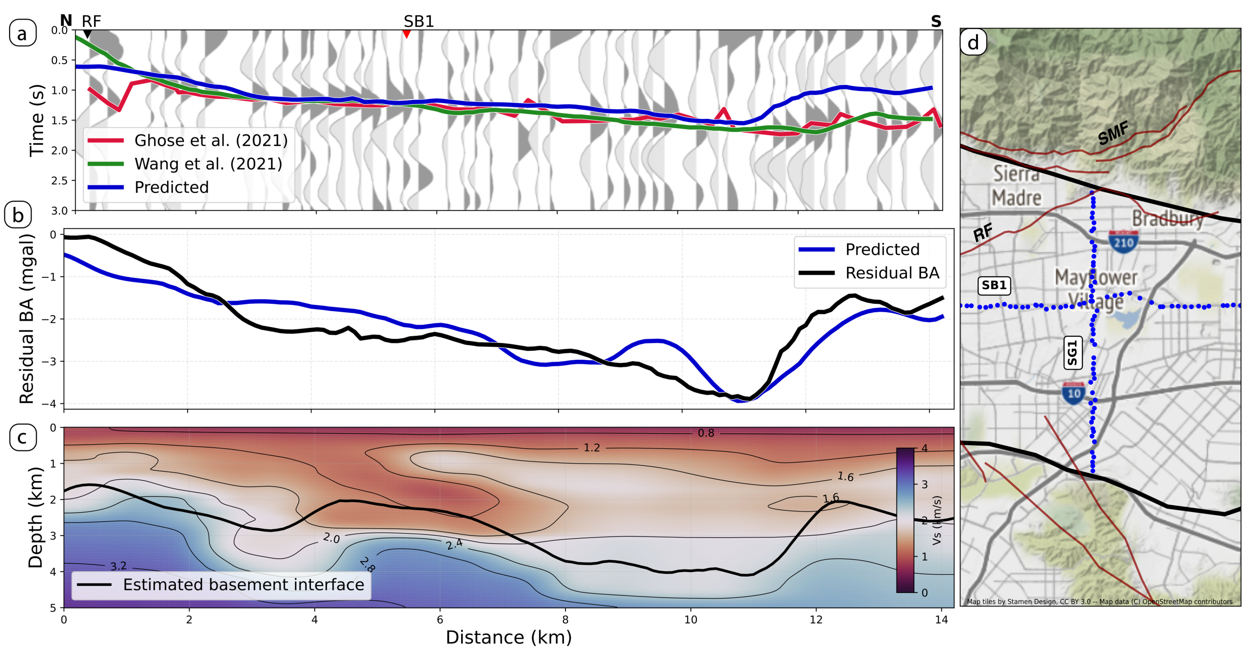

Figure 4. a) Profile along SG1 showing the time-to-basement from two RF studies and the predicted time-to-basement from this study. RF background from Ghose et al. (2022) is from a single event. b) Residual and predicted Bouguer anomaly is shown with black and blue lines, respectively. c) Shear wave velocity cross-section from Li et al. (2022) and the estimated basement surface determined by converting the blue line in a) to depth. d) Map showing the nodal stations of the SG1 line as blue dots. SB1 stations are included for reference. Maroon lines are fault locations. SMF, Sierra Madre fault; RF, Raymond fault.

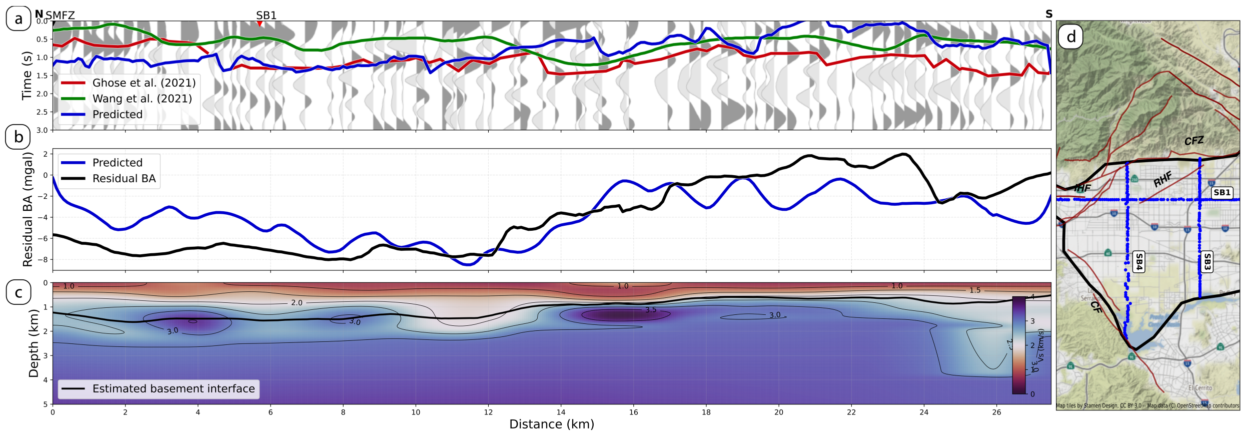

Figure 5. a) Profile along SB4 showing the time-to-basement from two RF studies and the predicted time-to-basement from this study. RF background from Ghose et al. (2022) is from a single event. b) Residual and predicted Bouguer anomaly is shown with black and blue lines, respectively. c) Shear wave velocity cross-section from Li et al. (2022) and the estimated basement surface determined by converting the blue line in a) to depth. d) Map showing the nodal stations of the SB4 line as blue dots. SB1 and SB3 stations are included for reference. Maroon

lines are fault locations. CF, Chino Fault; CFZ, Cucamonga Fault; IHF, Indian Hill Fault; RHF, Red Hill Fault.

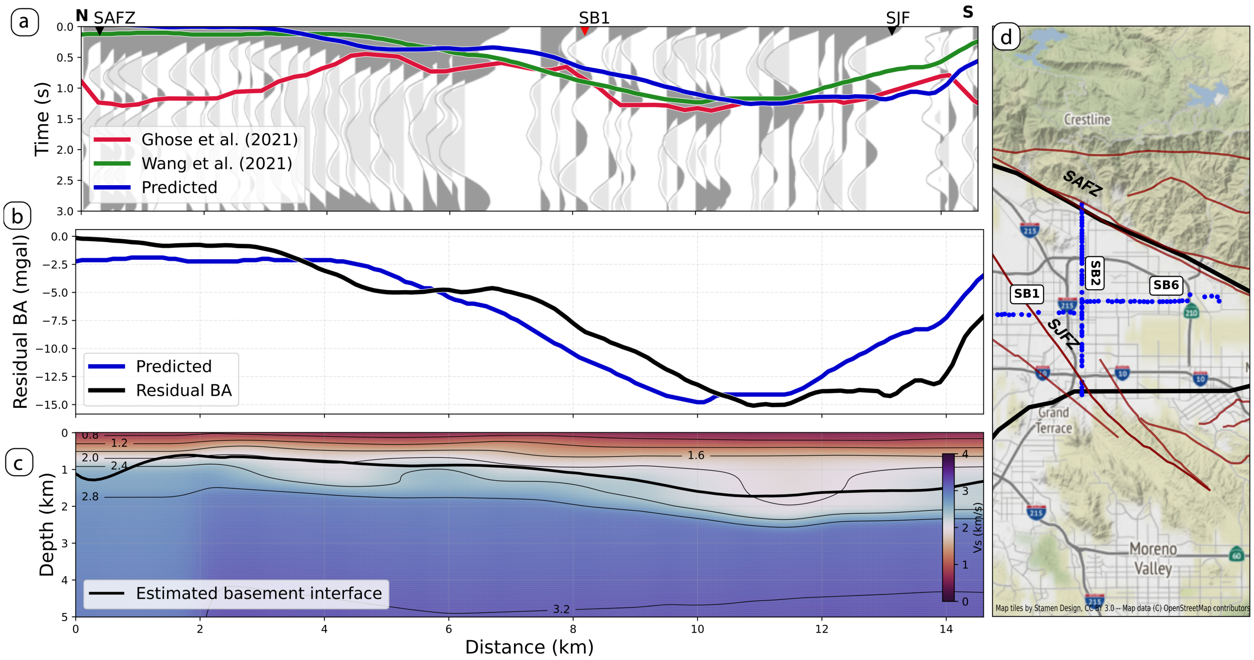

Figure 6. a) Profile along SB2 showing the time-to-basement from two RF studies and the predicted time-to-basement from this study. RF background from Ghose et al. (2022) is from a single event. b) Residual and predicted Bouguer anomaly is shown with black and blue lines, respectively. c) Shear wave velocity cross-section from Li et al. (2022) and the estimated basement surface determined by converting the blue line in a) to depth. d) Map showing the nodal

stations of the SB2 line as blue dots. SB1 and SB6 stations are included for reference. Maroon lines are fault locations. SAFZ, San Andreas Fault Zone; SJFZ, San Jacinto Fault Zone.

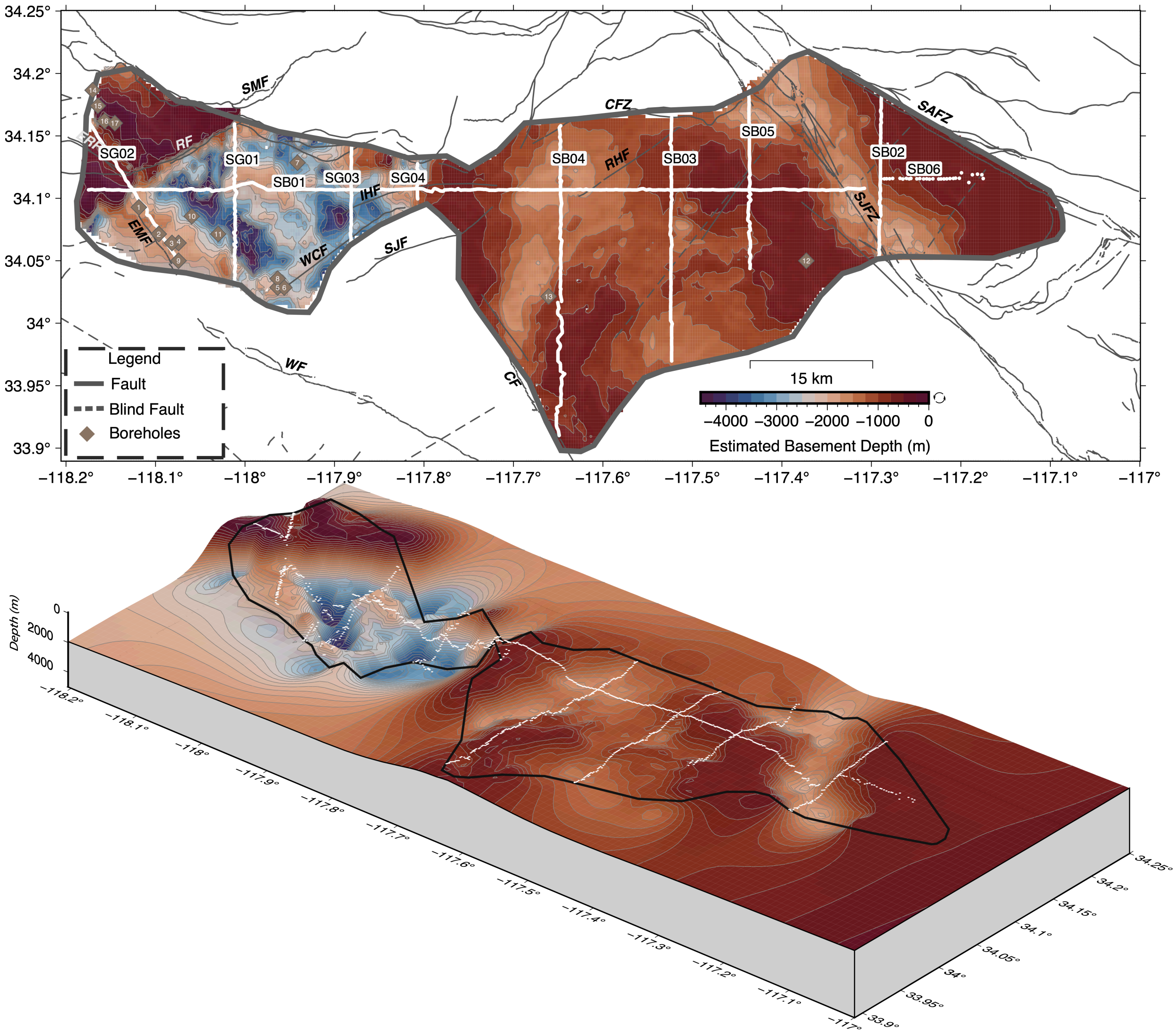

Figure 7. a) Depth to basement map of the greater Los Angeles area's San Gabriel, Chino, and San Bernardino. The borehole numbers correspond to those listed in Table S1. b) Three-dimensional perspective view from the southeast of the basin depth map. Basement depths are unconstrained outside the region shown in a). The surface shows the depth in meters below sea level. Small white circles represent the 10 nodal lines of the BASIN survey. The dark gray line outlines the study area and encompasses the three basins. Solid black lines are faults and dashed black lines are blind faults. CF, Chino Hill Fault; CFZ, Cucamonga Fault Zone; EMF, East Montebello Fault; ERF, Eagle Rock Fault; IHF, Indian Hill Fault; RCF, Rialto Colton Fault; RF, Raymond Fault; RHF, Red Hill Fault; SAFZ, San Andreas Fault Zone; SJF, San Jose Fault; SJFZ, San Jacinto Fault Zone; SMF, Sierra Madre Fault; WCF, Walnut Creek Fault; WF, Whittier Fault.

AGU PUBLICATIONS

Journal of Geophysical Research: Solid Earth

Supporting Information for

Three-Dimensional Basin Depth Map of the Northern Los Angeles Basins from Gravity and Seismic Measurements

V. Villa[1], Y. Li[1], R. W. Clayton[1], and P. Persaud[2]

[1]California Institute of Technology, Pasadena, CA, 91125. [2]Louisiana State University, Baton Rouge, LA, 70803.

Contents of this file

Figures S1 to S5
Tables S1

Introduction

The supporting information includes 5 out of the 10 lines mentioned in the manuscript. Lines SG3, SG4, SB3, SB5, and SB6 are shown here. Each figure shows the receiver function profile and the time-to-basement interpretations of Ghose et al. (2022) and Wang et al. (2021). The Bouguer gravity and residual Bouguer gravity values are shown. The shear-wave velocity model from Li et al. (2022) used to calculate the basement depth is shown and the basement depth is shown. For reference to each of the line's locations, a map with relevant fault locations is included.

Table S1 outlines the boreholes used to constrain the depth of the basement. The units of depth are in meters. The unique well number, or API, is provided for detailed information on the borehole's data.

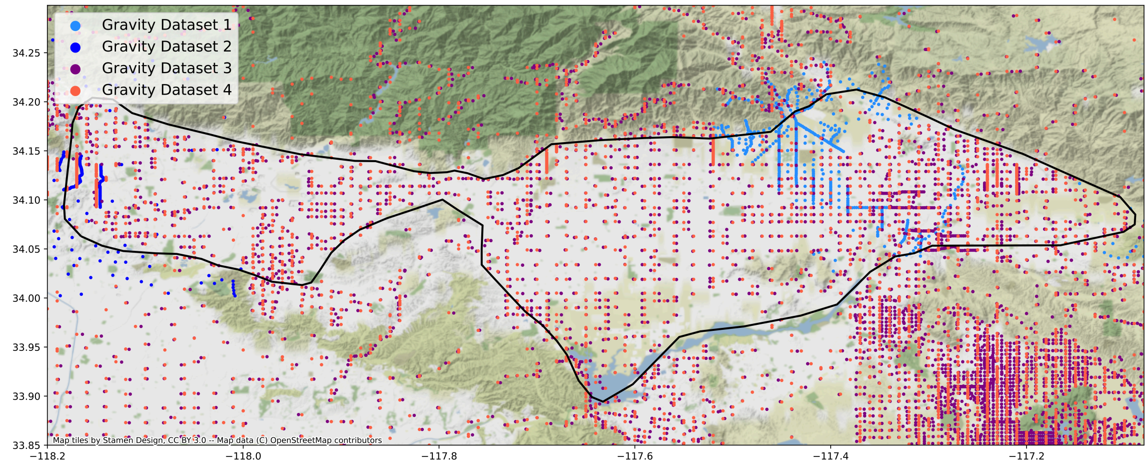

Figure S1. Gravity data set stations were obtained from (*PACES*, 2012). Individual data set stations are colored in different colors.

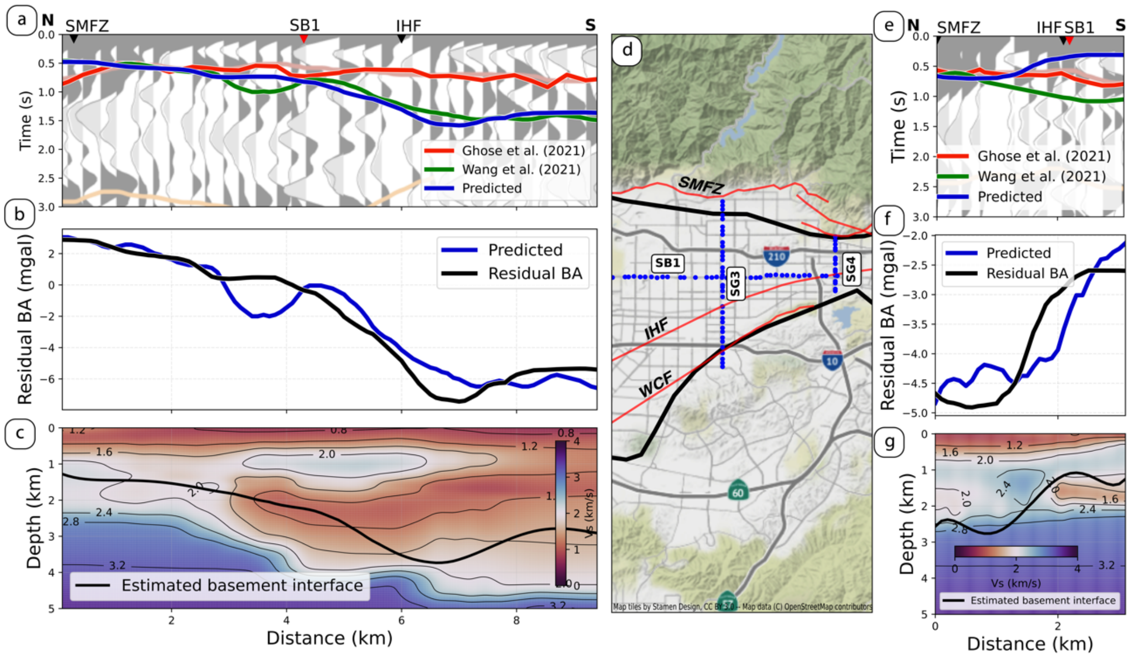

Figure S2. a) Profile along SG3 showing the time-to-basement from two RF studies and the predicted time-to-basement from this study. RF background from Ghose et al. (2022) is from a single event and the faint yellow line is an intra-crustal layer. b) Residual and predicted Bouguer anomaly is shown with black and blue lines, respectively. c) Shear wave velocity cross-section from Li et al. (2022) and the estimated basement surface determined by converting the blue line in a) to depth. d) Map showing the nodal stations of the SG3 and SG4 lines as blue dots. SB1 stations are included for reference. Maroon lines are fault locations. IHF, Indian Hill Fault; SMFZ; Sierra Madre Fault Zone; WCF, Walnut Creek Fault. e) Profile along SG4 showing the time-to-basement from two RF studies and the predicted time-to-basement from this study. RF background from Ghose et al. (2021) is from a single event. f) Residual and predicted Bouguer anomaly is shown with black and blue lines, respectively. g) Shear wave velocity cross-section from Li et al.

(2022) and the estimated basement surface determined by converting the blue line in e) to depth.

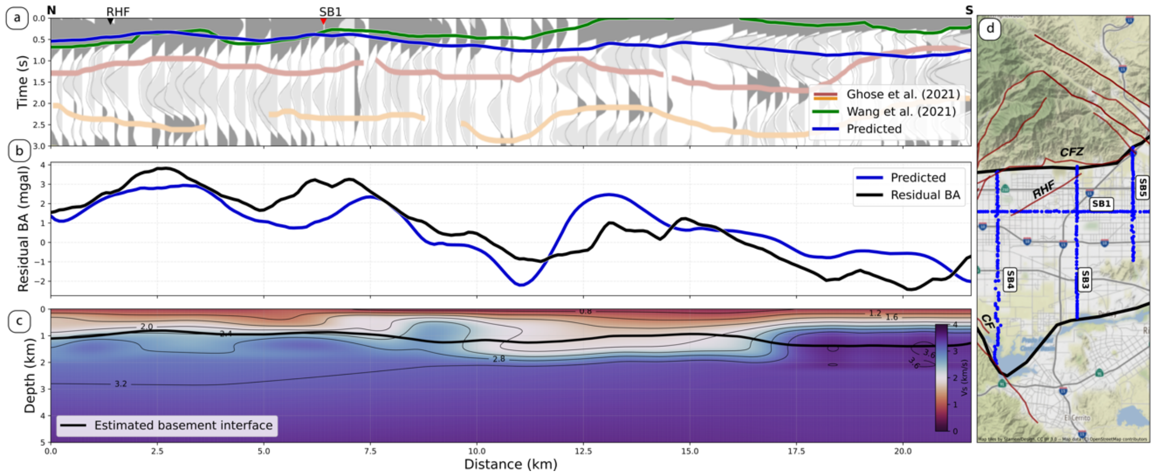

Figure S3. a) Profile along SB3 showing the time-to-basement from two RF studies and the predicted time-to-basement from this study. RF background from Ghose et al. (2022) is from a single event and the faint yellow line is an intra-crustal layer. b) Residual and predicted Bouguer anomaly is shown with black and blue lines, respectively. c) Shear wave velocity cross-section from Li et al. (2022) and the estimated basement surface determined by converting the blue line in a) to depth. d) Map showing the nodal stations of the SB3 line as blue dots. SB1, SB4, and SB5 stations are included for reference. Maroon lines are fault locations. CF, Chino Fault; CFZ, Cucamonga Fault Zone; RHF, Red Hill Fault.

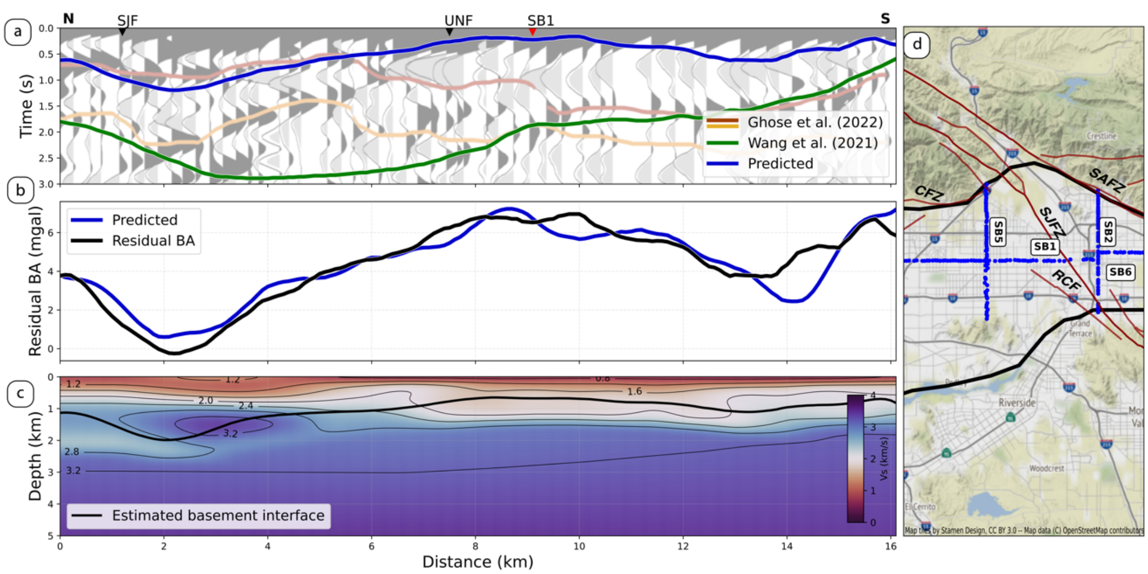

Figure S4. a) Profile along SB5 showing the time-to-basement from two RF studies and the predicted time-to-basement from this study. RF background from Ghose et al. (2022) is from a single event and the faint yellow line is an intra-crustal layer. b) Residual and predicted Bouguer anomaly is shown with black and blue lines, respectively. c) Shear wave velocity cross-section from Li et al. (2022) and the estimated basement surface determined by converting the blue line in a) to depth. d) Map showing the nodal stations of the SB5 line as blue dots. SB1, SB2, and SB6 stations are included for reference. Maroon lines are fault locations. CFZ, Cucamonga Fault Zone; RCF, Rialto Colton Fault; SAFZ, San Andreas Fault Zone; SJFZ, San Jacinto Fault Zone.

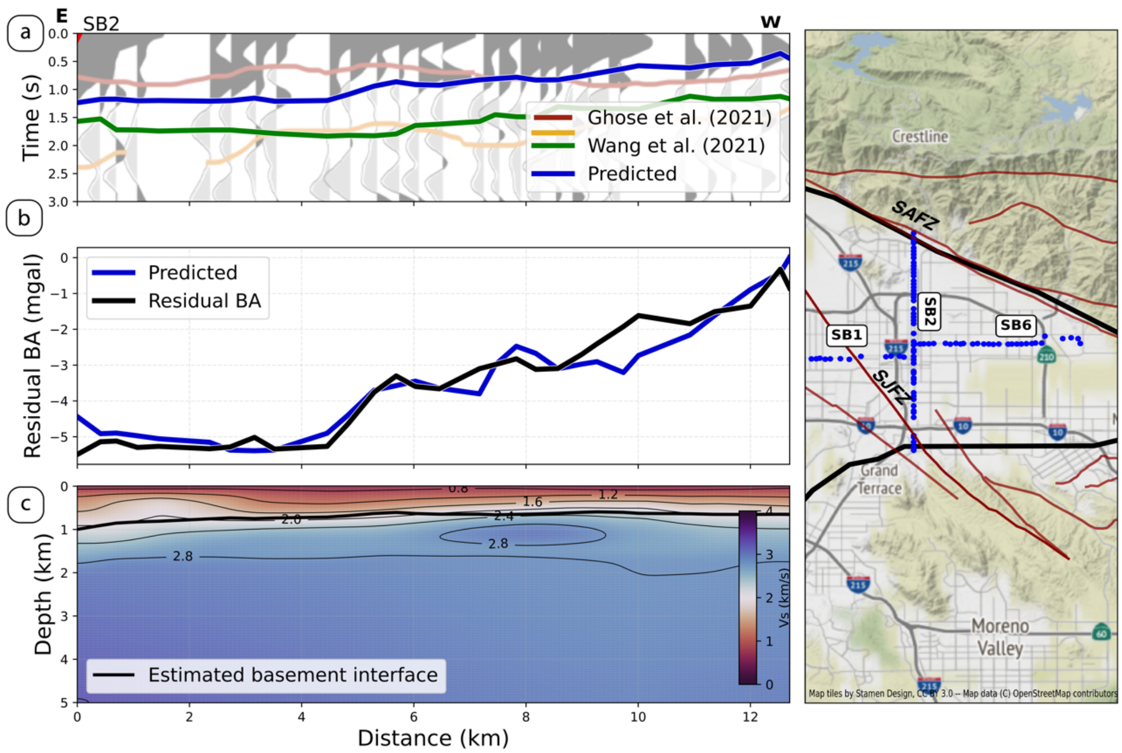

Figure S5. a) Profile along SB6 showing the time-to-basement from two RF studies and the predicted time-to-basement from this study. RF background from Ghose et al. (2022) is from a single event and the faint yellow line is an intra-crustal layer. b) Residual and predicted Bouguer anomaly is shown with black and blue lines, respectively. c) Shear wave velocity cross-section from Li et al. (2022) and the estimated basement surface determined by converting the blue line in a) to depth. d) Map showing the nodal stations of the SB6 line as blue dots. SB1 and SB2 stations are included for reference. Maroon lines are fault locations. SAFZ, San Andreas Fault Zone; SJFZ, San Jacinto Fault Zone.

	Name	**API**	**Well Depth (m)**	**Modeled Depth (m)**
1	Southern Pacific	0403706338	723	1600
2	South San Gabriel	0403705501	1402	1800
3	Harmon	0403705790	1790	1850
4	Cordova	0403720575	1798	1800
5	Puente One	0403706114	1812	2200
6	Puente Nine	0403706115	1800	1800

7	Consolidated	4003705962	2170	2900
8	McGinnis	4003706092	2301	2050
9	Rosemead	0403720665	2590	1950
10	El Monte	0403721403	2616	3350
11	Ferris	0403705964	3715	3050
12	Dana	0407100024	542	750
13	Donald B. Lamond	0407100083	725	1000
14*	C-68	Buwalda (1940)	228	228
15*	C-10s	Buwalda (1940)	243	243
16*	C-17	Buwalda (1940)	251	251
17*	C-127	Buwalda (1940)	350	350

Table S1. Boreholes were used in the study to calibrate and validate the model. The numbering indicates the location in figure 7. Wells 1-13 were obtained through the CalGEM website and are searchable through this API number. Wells 14-17 were obtained from Buwalda's (1940) report.

* Wells used to calculate depth for the Raymond Basin.

References

Buwalda, J. P. (1940). *Geology of the Raymond Basin* (pp. 1–131). California Institute of Technology. http://doi.org/10.22002/D1.20258

Ghose, R., Persaud, P., Wang, X., & Clayton, R. W. (2022). *High-frequency receiver function profiles reveal sedimentary basin structure beneath the northern Los Angeles area* [In-preparation].

Li, Y., Villa, V., Clayton, R., & Persaud, P. (2022). *Shear Wave Velocities in the San Gabriel and San Bernardino Basins, California* (world). https://doi.org/10.1002/essoar.10512118.1

PACES. (2012). Pan-American Center for Earth and Environmental Studies. http://gis.utep.edu/paces/PACES%20Gravity%20Magnetics.htm

Wang, X., Zhan, Z., Zhong, M., Persaud, P., & Clayton, R. W. (2021). Urban Basin Structure Imaging Based on Dense Arrays and Bayesian Array-Based Coherent Receiver Functions. *Journal of Geophysical Research: Solid Earth*, *126*(9). https://doi.org/10.1029/2021JB022279